Materials and Design 198 (2021) 109289

Contents lists available at ScienceDirect

Materials and Design

journal homepage: www.elsevier.com/locate/matdes

Plastic deformation throughout strain-induced phase transformation in additively manufactured maraging steels

SeyedAmirReza Shamsdini [a,*], M.H. Ghoncheh [a], Mehdi Sanjari [a,b], Hadi Pirgazi [c], Babak Shalchi Amirkhiz [b,a], Leo Kestens [c], Mohsen Mohammadi [a]

[a] Marine Additive Manufacturing Centre of Excellence, University of New Brunswick, Fredericton, NB E3B 5A1, Canada
[b] CanmetMATERIALS, Natural Resources Canada, Hamilton, ON L8P 0A5, Canada
[c] Department of Electromechanical, Systems and Metal Engineering, Ghent University, Ghent, Belgium

HIGHLIGHTS

- After the phase transformation retained γ remains along the cell boundaries, and the area is enriched by the solute atoms
- Strain-induced phase transformation is responsible for the variation of strain hardening rate under uniaxial tensile test
- The fracture area shows a fully martensitic structure, fine grains, a high fraction of LAGBs and high dislocation density

GRAPHICAL ABSTRACT

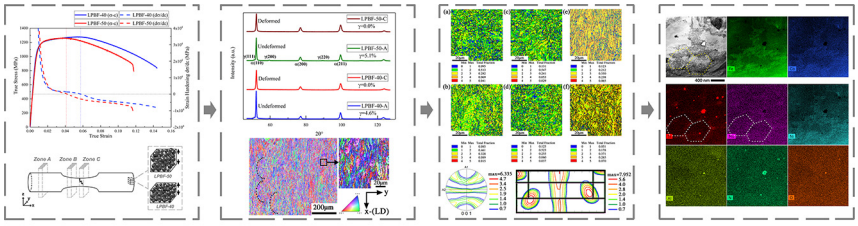

ARTICLE INFO

Article history:
Received 7 October 2020
Received in revised form 29 October 2020
Accepted 31 October 2020
Available online 2 November 2020

Keywords:
18Ni-300 Maraging steel
Laser powder bed fusion (LPBF)
Layer thickness
Austenite (γ)
Martensite (α)

ABSTRACT

A comprehensive study was intended to show the microstructural features of additively manufactured (AM) 18Ni-300 maraging steel. Uniaxial tensile tests were conducted on specimens built using laser powder bed fusion (LPBF) technique for two different powder layer thicknesses. The specimens were built to have the lowest possible porosity, and tensile tests showed two stages of strain hardening. In stage I, the dislocation density increased, leading to a positive strain hardening rate. A negative strain hardening rate due to the necking effect was then followed in stage II. X-ray diffraction (XRD) analyses revealed a phase transformation through the deformation. Various analyses via electron backscattered diffraction (EBSD) technique was then conducted with large scans over three different zones representing undeformed, deformed, and severely deformed close to the fracture area. The pole figures and orientation distribution functions (ODF) revealed a texture evolving through the deformation process in agreement with the kernel average misorientation (KAM) and grain boundary maps. Transmission electron microscopy (TEM) was used to detect the inclusions and segregated alloying elements adjacent to the fractured surfaces. Results indicated that the deformation led to diminishing the austenite (γ) phase, while the transformed austenite sourced the high dislocation density area at cell boundaries.

1. Introduction

Additively manufactured (AM) maraging steels have been recently received considerable attention due to their superior mechanical properties as well as their excellent manufacturability [1]. Coexistence of the martensite (α) phase and well-dispersed nano-precipitates results in ultra-high-strength and hardenability accompanied by a high level of machinability, which is attractive to the automotive and aerospace industries [2]. Over the last couple of years, the progress in laser additive manufacturing in terms of machine capabilities and process parameters has led to the development of products with exceptional mechanical properties compared to conventional counterparts [3]. In this regard, optimization of the process parameters brings a higher probability of

* Corresponding author.
E-mail address: sshamsdi@unb.ca (S. Shamsdini).

https://doi.org/10.1016/j.matdes.2020.109289

soundness in the product by lowering the volume fraction of structural defects, e.g. hot cracking, keyholes, shrinkage, and gas porosities [4].

In AM maraging steels, reheating cycles during consecutive powder layer depositions induces a quasi-dynamic ageing phenomenon [5]. This artificial ageing results in the formation of fine precipitates through the heat-affected zones, and subsequently, higher strength of the as-built AM product compared to the conventionally cast parts [6]. Despite the comprehensive studies on the heat-treated AM samples [5–8], the microstructural and mechanical behaviour of the as-built products has been overlooked. The as-built product mainly contains the body-centred cubic (BCC) martensite (ά) and a small fraction of the face-centred cubic (FCC) austenite (γ) phase [5]. According to the Fe–Ni phase diagram, at almost 18 wt% Ni, γ is thermodynamically stable over a wide temperature range between the peritectic (1716 °C) and eutectoid (688 °C) transformations, while the ά phase is expected to athermally form from γ at temperatures below 870 °C [9,10]. Due to the high contents of Ni as a strong γ-stabilizer and ultra-high cooling rate during laser powder bed fusion (LPBF), a small portion of retained γ is always expected to remain at ambient temperatures [8]. This phase can be nucleated and grown during the ageing process as well, known as reverted γ [11]. The higher amount of reverted austenite results in higher ductility and toughness and prevents premature failure [12]. The amount of retained γ inversely affects the strength and hardness of the as-built maraging steel, while increases its ductility [13] [14]. The plastic deformation, on the other side, can also cause γ → ά transformation [15] [16]. The strain-induced phase change, also known as transformation induced plasticity (TRIP), was previously studied in the Fe-Cr-C system, and the role of reverted austenite on stopping cracks from penetrating the martensite laths was discussed [12].

The AM maraging steels typically show a hierarchical grain structure, where the ά laths form inside the prior austenite grains (PAG) in the style of blocks and packets [17] [18]. Besides, a synergy between consecutive reheating cycles and rapid cooling during the LPBF process leads the grains to grow along the build direction and perpendicular to the melt-pool boundaries [19] [20]. This directional growth leads to anisotropy, which is another reason for higher mechanical strength perpendicular to the building direction compared to the conventional manufacturing methods [21]. The plastic deformation as another factor affecting the grain structure is also needed to take into account. Multiple studies have been conducted to discuss the effects of texture evolution during deformation in 18Ni maraging steels [9] [22] [23] [24]. Reis et al. [9] observed the martensite to austenite phase transformation due to creep for 18Ni maraging steel resulting in ductile failure. Ahmed et al. [22] performed a deformation study on cold-rolled 18Ni maraging steel studying the magnetic properties due to phase transformation. Beres et al. [23] investigated the hydrogen embrittlement of maraging steels and concluded that the austenite grain size affects the failure mechanism. Figueiredo et al. [24] studied the texture of the forged 18Ni maraging steel in different depths from the forged surface. They observed an increase in the α and γ fibres with increasing depth as well as the lowest strain in the surface.

Due to the novelty of the AM process compared to conventional manufacturing methods, a thorough study on the deformation of additively manufactured products is needed. The mutual effect of the AM process and plastic deformation on the strain-induced phase transformation and mechanical behaviour of the as-built AM 18Ni-300 maraging steel has been conducted in the current study. In order to investigate the role of the AM process, the powder layer thickness is chosen as a variable parameter, while the effect of plastic deformation is recognized by employing the uniaxial tensile testing. Since the volume fraction of retained γ is different between the AM and conventionally cast steels [8], the TRIP effect of the AM 18Ni-300 maraging steel is necessary to be evaluated. Thus, a thorough study on the strain-induced phase transformation in the as-built 18Ni-300 maraging steel is investigated in this research.

2. Experimental procedure

2.1. Material and manufacturing process

Gas atomized 18Ni-300 maraging steel powder was deposited to produce horizontally printed cylindrical bars via an EOS M290 machine. The chemical composition of the powder is given in Table 1. A scanning beam with 100 μm spot size was emitted by a 400 W Yb-fibre gun during the manufacturing process, and pure nitrogen gas (99.999%) was continuously purged into the chamber. The LPBF technique was chosen to deposit and fuse powder layers on a build plate preheated at 40 °C, where a 67° strip scanning strategy was applied between successive layers. Powder deposition was carried out at two powder layer thicknesses of 40 μm and 50 μm (designated as LPBF-40 and LPBF-50) to fabricate the cylindrical bars with 12 mm and 120 mm in diameter and length, respectively. The laser power and scanning speed used for LPBF-40 samples were 285 W and 960 mm/s, while the LPBF-50 samples were made using 305 W power and 1010 mm/s scanning speed. The hatch distancing of 110 μm was used for both cases.

A mapping technique was used to measure the porosity. In this method, the polished surface's optical microscopy (OM) image was analyzed and based on the contrast between the base metal and the pores, the porosity fraction was calculated. High magnification images were collected through a Zeta-20 OM, and the area fraction was measured over the entire surface. The top surface was ground and polished, and the measurement was conducted over multiple layers through the depth. The average value was reported as the overall porosity level.

2.2. Sample preparation and tensile testing

Specimens for the uniaxial tensile testing were machined according to the E8/E8M ASTM standard [26]. Through a quasi-static strain rate, the tensile tests were performed using a universal hydraulic Instron 1332 machine. The elongation was measured using a 25 mm extensometer at a 9×10^{-3} s^{-1} strain rate, and the tests were conducted at room temperature. As shown in Fig. 1, the building direction along the z-axis was perpendicular to the loading direction. Samples were cross-sectionally cut into three pieces of undeformed (zone A), deformed (zone B), and severely deformed (zone C) via an electrical discharge machine (EDM). In this regard, the undeformed piece was collected from the part fixed within the grips, while the deformed and severely deformed pieces were taken from locations near the gauge shoulder and fracture area. Afterward, samples were mounted, ground through 300–4000 grits SiC sandpapers, and regularly polished using 6.0–0.05 μm polish cloths.

2.3. Phase identification

X-ray diffraction (XRD) technique was used to identify phases in the samples collected from A and C zones. A Brucker D8 instrument with a Co-K_α radiation source working at 45 mA and 35 kV was used to collect the data over $45 < 2\theta < 130°$ with a rotation speed of 60 deg./min, and the intensity of peaks was measured using the Rietveld analysis technique.

2.4. Electron microscopy

EBSD measurements were conducted using an FEI QuantaTM 450 FEG-SEM microscope to study the grain size and orientation and the area fraction of low- and high-angle grain boundaries (LAGBs and HAGBs) in zones A, B, and C. The EBSD studies were carried over a zone within 1400×500 μm^2 with a step size of 500 nm located at the x-y plane specified in Fig. 1. The diffraction patterns were also collected using the TSL® OIM data collection software and were post-processed by the OIM data analysis software. The crystallographic textures were calculated by harmonic series expansion with truncation at $L = 16$.

Table 1
Chemical composition of the powder used in the DMLS process [25].

Element	Fe	Ni	Co	Mo	Ti	Al	Cr	Cu	C	Mn	Si	P	S
Max %	Bal.	19.00	9.50	5.20	0.80	0.15	0.50	0.50	0.03	0.10	0.10	0.01	0.01
Min %	Bal.	17.00	8.5	4.50	0.60	0.05	–	–					

Regarding the transmission electron microscopy (TEM), an FEI Helios NanoLab 650 dual beam instrument was utilized to collect a thin piece of the sample at the vicinity of the fracture area (zone C). The effect of plastic deformation on the volume fraction of the γ phase was assessed in detail with an FEI Tecnai Osiris TEM apparatus that was equipped with a 200 keV X-FEG gun.

3. Results

Fig. 2 shows the OM micrographs of the polished surfaces along with the average porosity levels. Fig. 2 (a) shows the LPBF-40 sample with a low fraction of porosity, while Fig. 2 (b) shows the LPBF-50 sample with a higher average porosity level compared to the former case. In both cases, the pores sizes are very small (under 50 μm), and the overall porosity level shows an almost fully dense material.

Fig. 3 shows the true stress-strain and strain hardening curves for the LPBF-40 and LPBF-50 samples. The LPBF-40 sample elucidates a combination of the higher ultimate tensile strength (UTS) and better ductility, which brings higher energy absorption before failure. The total strain and UTS values in the LPBF-40 and LPBF-50 are almost 14.39% - 1278 MPa and 11.76% - 1265 MPa, respectively. However, their stress-strain curves present a consistency within the initial 4% elongation, where the materials are exposed to elastic-homogeneous plastic loading condition. The difference in elongation percentage has mostly occurred after the peak stress, where the structural defects such as porosities and microcracks start to nucleate, coalesce and grow. It seems that the LPBF-40 structure is more integrated than the LPBF-50 one. As another observation, the LPBF-50 sample shows a sharp drop in its stress values right before the fracture. This trend was reported by Rusinek and Martinez [27] as a deformation step in which a high volume fraction of porosities is being coalesced to form microvoids. In the current study, a slight increase in the tensile strength compared to the literature was achieved, which is presented in Fig. 4 [5,28–30]. In this Figure, ultimate tensile strength versus the fracture strain is presented for 18Ni-300 maraging steels produced using both additive and conventional manufacturing techniques.

Due to the highly anisotropic texture resulted from the directional grain structure, the AM products typically show higher strength than those conventionally cast and solidified [29]. By focusing on the strain hardening curves, it is confirmed that change in the powder layer thickness does not affect the rate of strain hardening; however, it just shifts the critical point of $d\sigma/d\varepsilon = 0$ from 6% strain in the LPBF-40 sample to 4% in the LPBF-50 one. This point is following the peak stress where a balance between strain hardening and geometric softening takes place.

Fig. 5 illustrates the EBSD results of the LPBF-40-A and LPBF-50-A samples, including inverse pole figures, orientation distribution function (ODF), and pole figures (PF) of the texture analyses. The inverse pole figures show the melt-pool boundaries (curved dash lines) and the crystallographic orientation of grains over a large scan area. The orientation is random for both cases, which can be attributed to grains renucleation during repetitive reheating cycles. As a comparison between two structures, the LPBF-40-A contains a combination of grains oriented along the ⟨100⟩ and ⟨111⟩ directions, while the LPBF-50-A reveals a higher fraction of grains preferentially oriented along the ⟨100⟩ direction. The (001) pole figures in Fig. 5 (c, d) show peaks in the center in both cases. The pole figures are in agreement with the ODF plots shown in Fig. 5 (e, f). In Fig. 5 (e, f), highly intensified components of {100} θ-fibre are observed. The {111} γ-fibre components are intensified in the LPBF-40-A samples. However, the LPBF-50-A shows weaker γ-fibre components comparatively.

Fig. 6 shows the XRD patterns for the undeformed and severely deformed samples for both cases of powder layer thickness. The LPBF-40-A sample is reported to have a lower γ volume fraction (4.6%) than the LPBF-50-A case (5.1%). The γ peaks shown in Fig. 6 have been disappeared in the LPBF-C samples, in agreement with the elimination of the γ phase through the strain-induced $\gamma \rightarrow \acute{\alpha}$ phase transformation. It is noteworthy that, no traces of hcp-martensite were depicted in the

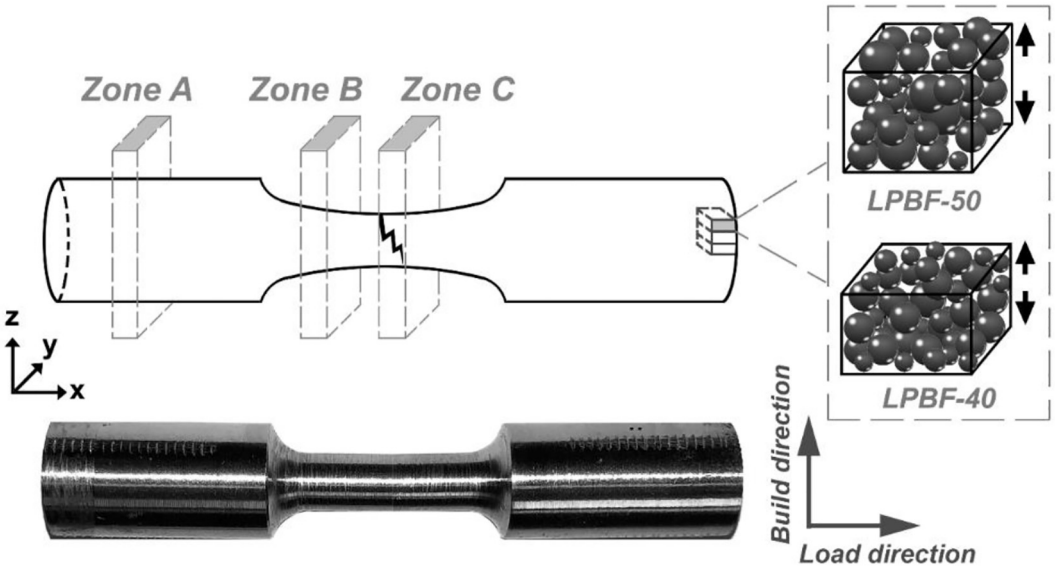

Fig. 1. Schematically design of the tensile test sample showing the powder layer thickness.

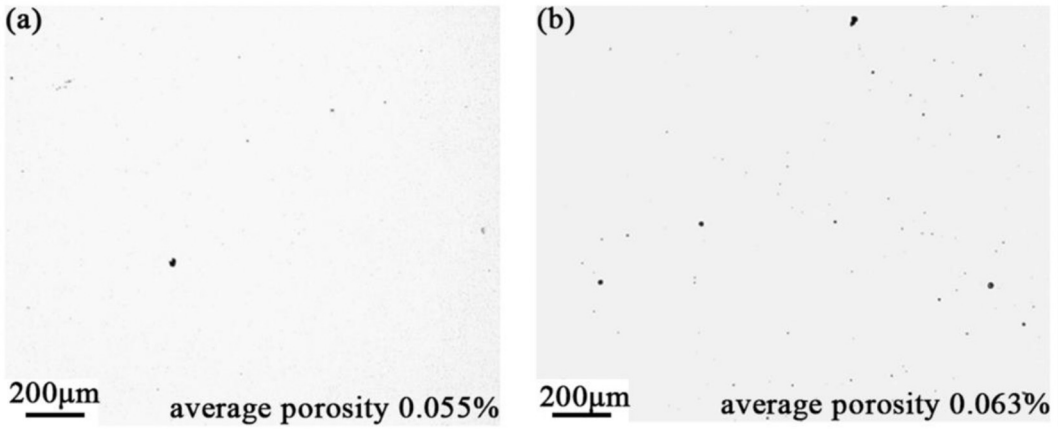

Fig. 2. OM micrographs showing porosity in (a): LPBF-40, (b): LPBF-50.

XRD patterns [15]. Although the maraging steel used in the current study has a substantially high percentage of alloying elements, it shows γ to the ά phase transformation due to plastic strain, similar to the low alloy ferritic bainitic steels (L-TRIP) [32]. It turns out that a strain-induced transformation can also prevent premature failure, while a complete transformation of γ to ά may occur in lower strains [12,13]. Similarly, in the current study, the material has gone through a complete phase transformation before the fracture.

Fig. 7 shows the collected EBSD data of zone B near the gauge shoulder, which is partially exposed to plastic deformation. Melt-pools are identified and marked in Fig. 7 (a, b) by curved dash lines. The size of the melt-pools is the same as those observed in zone A (Fig. 5). Like the undeformed cases in Fig. 5, components of the θ-fibre{100} and γ-fibre{111} are observed in the zone-B for both LPBF-40 and LPBF-50 samples. Although the pole figures that are shown in Fig. 7 (c) and (d) look similar, the intensities are weaker in the zone-B compared to zone-A (see Fig. 5). The {111} components observed in the ODF plot in Fig. 7 (e, f) are similar for both LPBF-40 and LPBF-50 cases and agree with the pole figure plots showing similar grain orientation for LPBF-40-B and LPBF-50-B samples.

Fig. 8 represents collective EBSD data of zone C, which is neighbouring to the fracture area. As shown in Fig. 8 (a, b), the grains are drawn along the load direction resulting in the semi-oval shape of the melt-pools. Fibrous textures are observed in the EBSD pole figures and shown in Fig. 8 (c, d). Fig. 8 (e, f) show the $\varphi 2 = 45°$ section of the ODF designated by θ-fibre {100} and γ-fibre {111} planes. The (111)[$1\bar{2}1$] and (111)[$\bar{1}\bar{1}2$] peaks show the θ-fibre components, while (001)[$1\bar{1}0$] and (001)[$\bar{1}\bar{1}0$] represent γ-fibre. The peaks in the {001} family planes are not a considerable concern due to the high vulnerability of

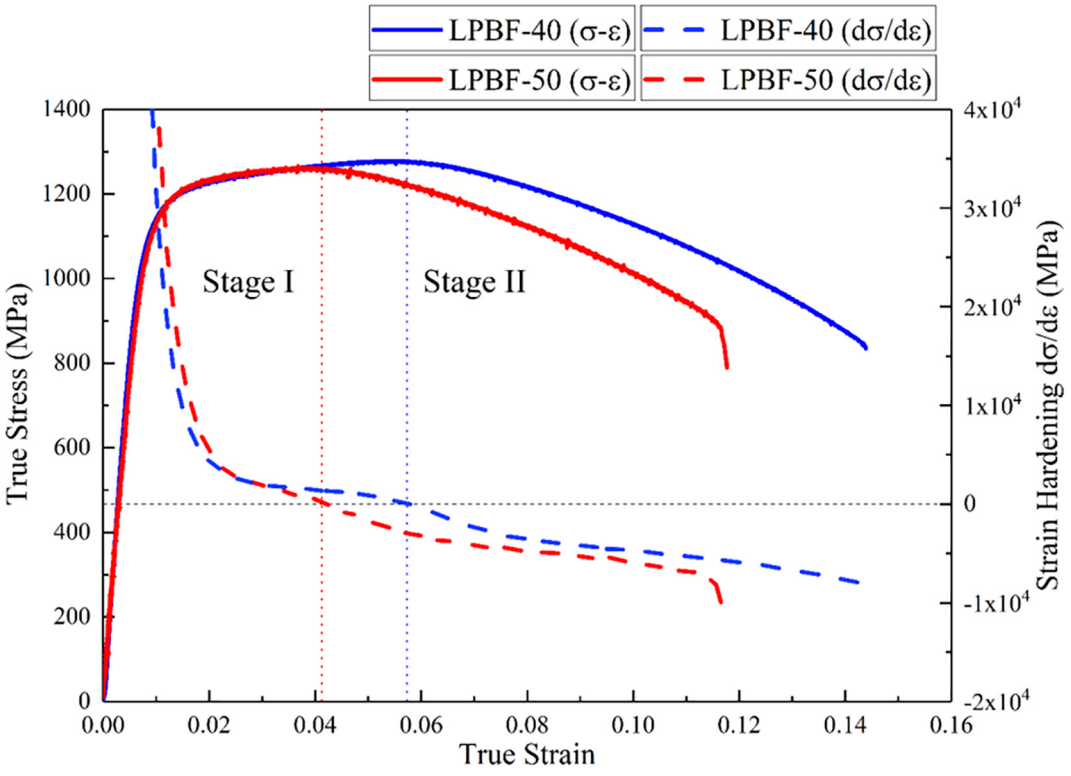

Fig. 3. Tensile stress-strain curves and the corresponding strain hardening variation.

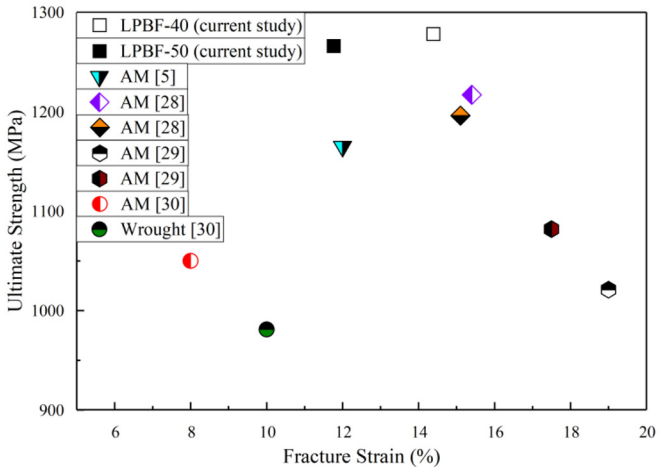

Fig. 4. Ultimate tensile strength versus fracture strain for 18Ni-300 maraging steels produced using both additive and conventional manufacturing techniques [5,28–30].

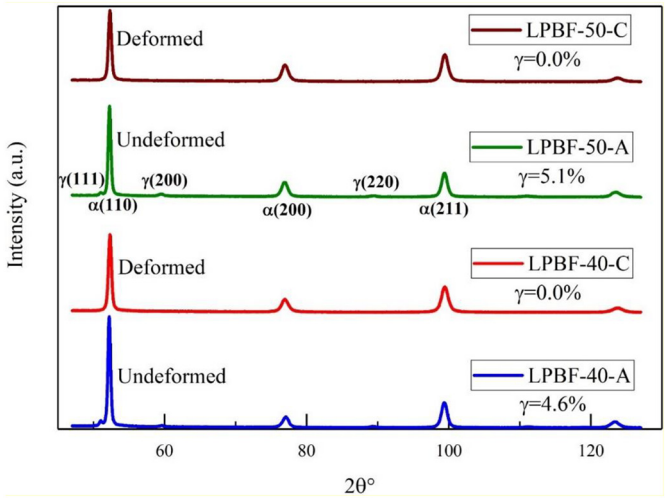

Fig. 6. XRD pattern for the 18Ni-300 deformed and undeformed samples in zones A and C.

these planes to crack propagation and transgranular cleavage fracture in the BCC structure [33]. It is also possible that the intergranular fracture initiates from the porosities at the vicinity of the cell boundaries and deflects through the {001} planes [23].

Fig. 9 displays the grain boundaries and the area fraction over different sectioned zones in the LPBF-40 and LPBF-50 samples. High angle grain boundaries (HAGBs) categorized as the 2D structural defect with 15–64.7° misorientation angles are pointed out in black colour, while

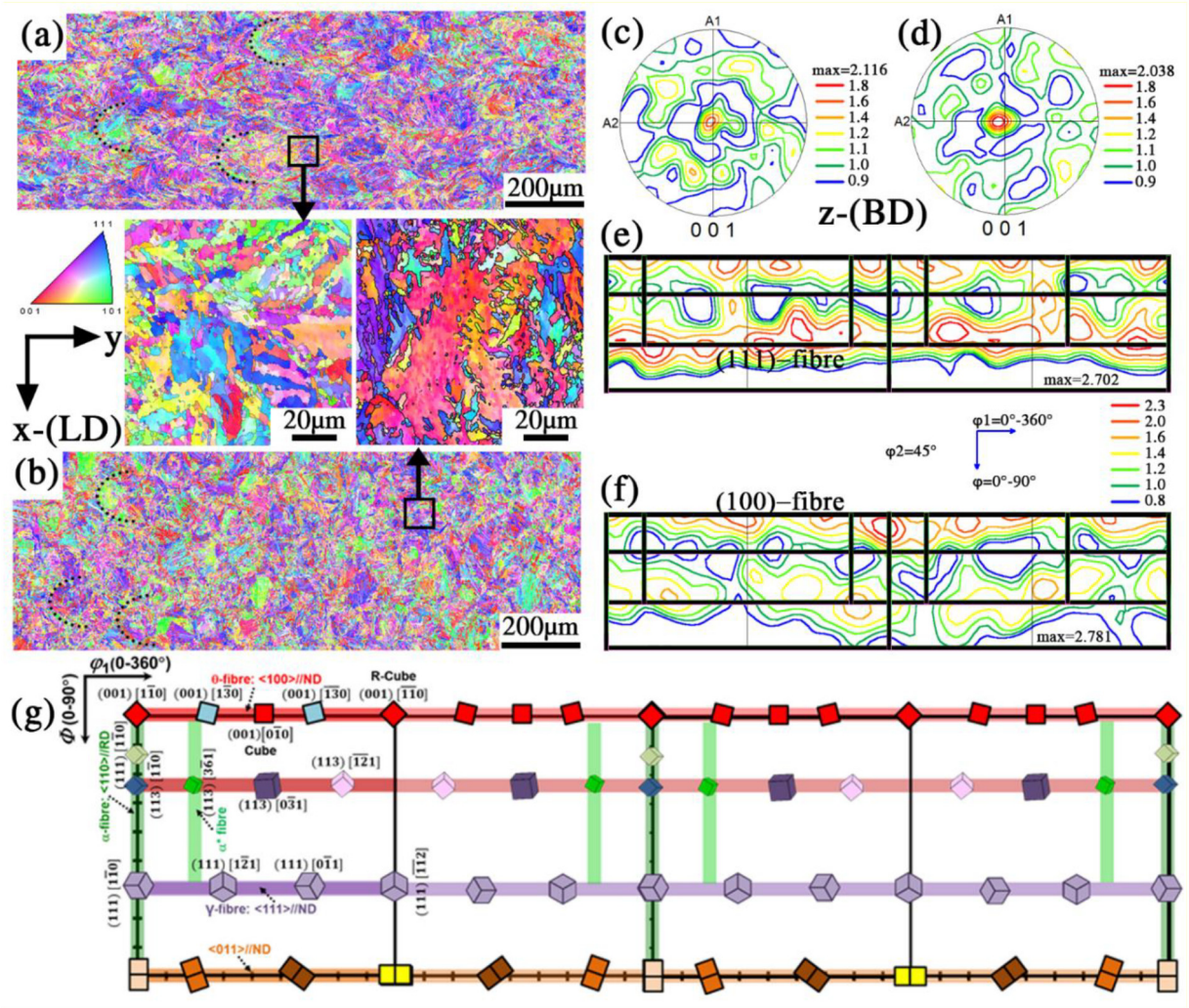

Fig. 5. (a, b): IPF of LPBF-40-A, LPBF-50-A, (c, d): Pole figures of LPBF-40-A and LPBD-50-A, (e, f): ODF of LPBF-40-A, LPBF-50-A, (g): ODF key components [31].

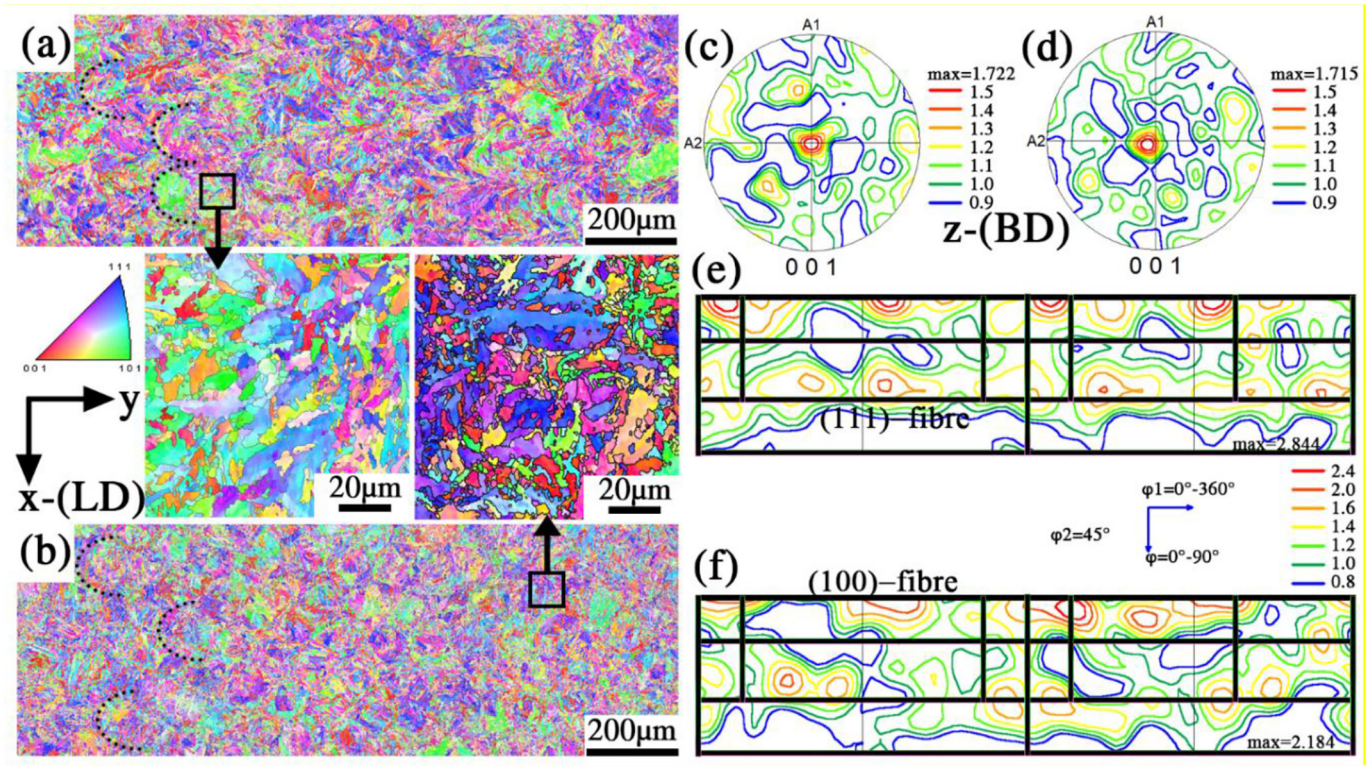

Fig. 7. (a, b): IPF of LPBF-40-B, LPBF-50-B, (c, d): Pole figures of LPBF-40-B and LPBD-50-B, (e, f): ODF of LPBF-40-B, LPBF-50-B.

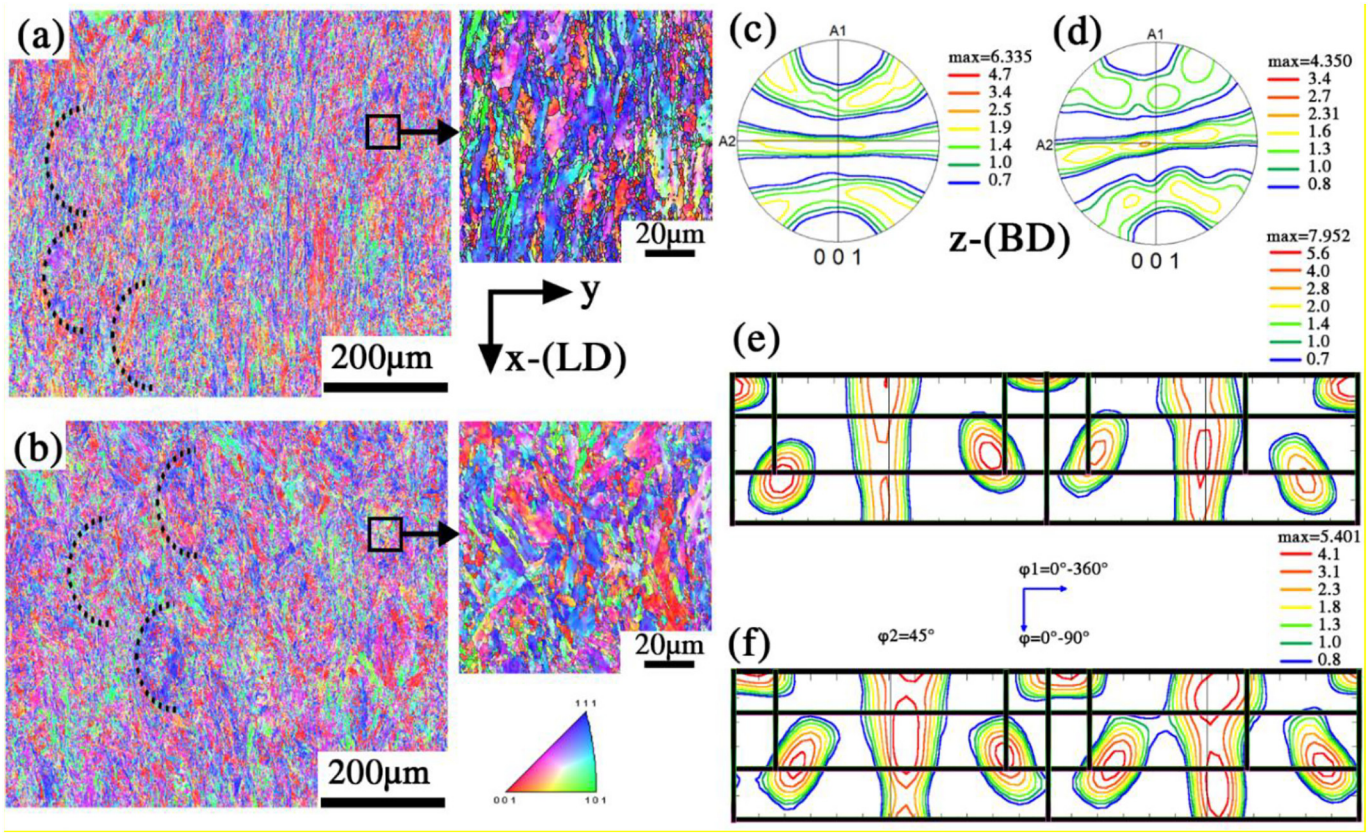

Fig. 8. (a, b): IPF for LPBF-40-C, LPBF-50-C, (c, d): Pole figures for LPBF-40-C and LPBD-50-C, (e, f): ODF for LPBF-40-C, LPBF-50-C.

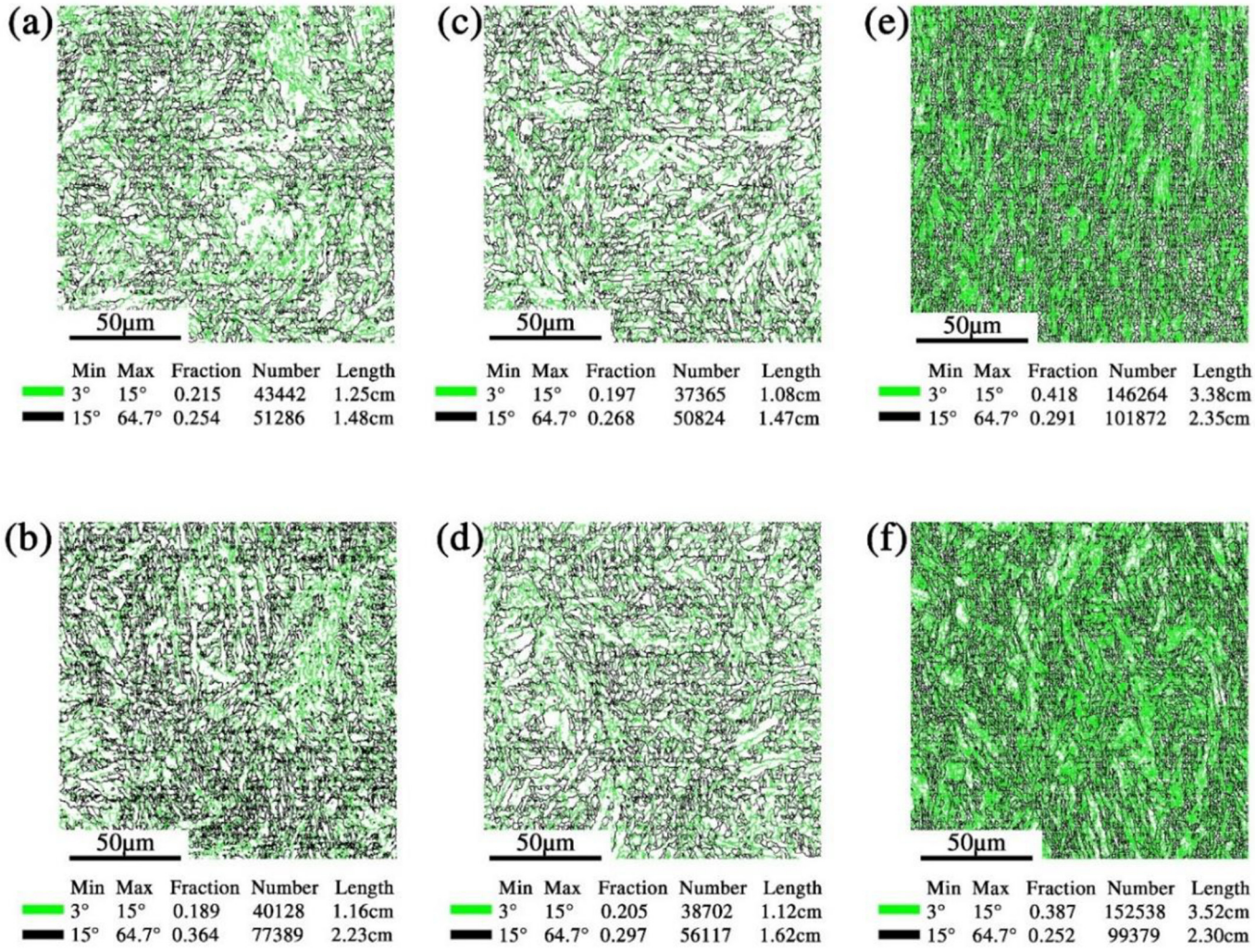

Fig. 9. EBSD grain boundary maps in three different zones shown for (a, b): LPBF-40-A, LPBF-50-A, (c, d): LPBF-40-B, LPBF-50-B, and (e, f): LPBF-40-C, LPBF-50-C.

low angle grain boundaries (LAGBs) with misorientation angles ranged within 3–15° are shown in light green colour. In both cases of the powder layer thickness, the plastic deformation results in more number and higher length of the LAGBs. As Sangid et al. showed [34], the GBs with lower interfacial energy, such as the values expected in LAGBs, offer a more substantial barrier against slip transmission. Regarding this fact, the as-built structure of the LPBF-40-A sample with a lower fraction of LAGBs compared to the LPBF-50-A zone is supposed to be more resistant against the dislocations slip during the uniaxial tensile testing. This trend is also observed in the deformed LPBF-B zones. Therefore, the LPBF-40 sample reveals more strain hardenability, which brings it a higher UTS value than the LPBF-50 one. The above observation is in good agreement with the results in Fig. 3. The LAGBs are suitable sites to accumulate and tangle the dislocations. Subsequently, an increase in the LAGBs in zone C is a shred of evidence showing the high density of dislocations in Fig. 9 (e, f) [35].

Fig. 10 shows Kernel Average Misorientation (KAM) technique in zones A-C. The KAM results are used to measure the local grain misorientation, where the more dislocation density leads to higher KAM values. It can also be employed to investigate the local lattice distortion, localized deformation, and stored strain energy in grains [36] [37]. The LPBF-40 and LPBF-50 samples in zones A and B present a semi-homogenous distribution of KAM majorly ranged at intermediate intensities (Min:1-Max:2). The LPBF-50-(A to C) samples show a localized distribution of KAM at higher intensities compared to the LPBF-40-(A to C). In the undeformed cases (zone A), the difference in KAM intensity can be hypothesized due to a difference in residual stresses stored during 40 μm- and 50 μm-thick powder layers depositions. Higher KAM values (Min:4-Max:5) in the LPBF-50-A imply that the stored energy during 50 μm-thick layers deposition is higher than the 40 μm case numerous LAGBs compromise it. Since the more residual stresses lead to more dislocations nucleation, and consequently, more stored internal energy, it can be hypothesized that the LPBF-50 undeformed structure contains a higher volume of residual stresses compared to the LPBF-40 one. It might be another reason behind the lower strength and ductility of the LPBF-50 samples. In zone C, the KAM intensity is higher, ranged within Min:3-Max:4. A higher fraction of intensified KAM values is again observable in the LPBF-50 sample compared to the LPBF-40 case.

In Fig. 11, the grain size distribution in each zone is presented for both LPBF-40 and LPBF-50 samples. As seen, the difference in powder layer thickness does not affect the grain size of the AM product. Zones A and B present similar trends in grain size variation, where the size of almost 90% of grains is below 10 μm. However, in the sample collected from the vicinity of the fracture area (zone c), the majority of grains (90%) is ranged below 6 μm in size. More specifically, around 50% of grains in the severely deformed zone C are smaller than 2 μm, while only 25–30% of the grains in zone A and B are below 3 μm. The average grain size is also measured and presented in Table 2.

The distribution of the misorientation angle in different zones is shown in Fig. 12. Fluctuation in data within 30°-60° range is higher in

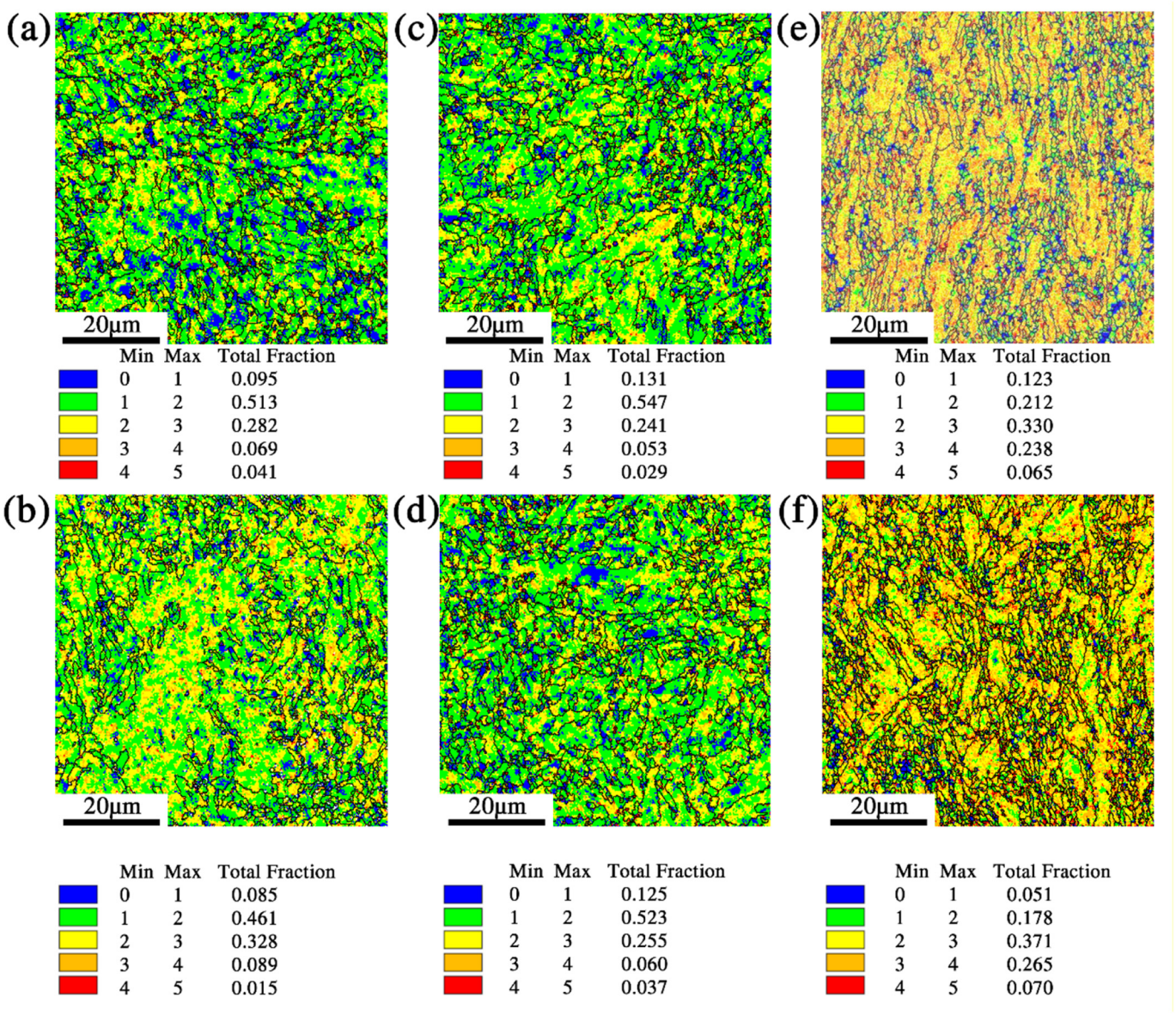

Fig. 10. EBSD KAM in three different zones shown for (a, b): LPBF-40-A, LPBF-50-A, (c, d): LPBF-40-B, LPBF-50-B, and (e, f): LPBF-40-C, LPBF-50-C.

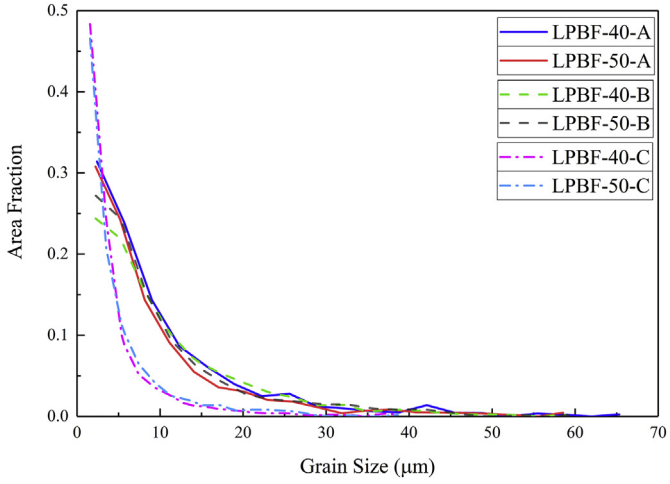

Fig. 11. Grain size distribution in different zones of the LPBF-40 and LPBF-50 samples.

the undeformed samples (collected from zone A). In all samples except the LPBF-40-C, an increase in the fraction of misoriented grain is marked close to 60°.

The STEM-BF image and corresponding elemental distribution maps of the LPBF-40-C and LPBF-50-C samples are shown in Figs. 13 and 14, respectively. According to distribution maps of Ti, N, Al, and O, the TiN and Al_2O_3 are determined as nanoparticles filling the pores that were made during the manufacturing process [14]. During the tensile deformation, those round Al_2O_3/TiN core/shell inclusions become elongated [14], and subsequently, debonding occurs at their interfaces. Since both inclusions have non-metallic (covalent) bonding through their structure and their surface wettability during the solidification (before any further deformation processes) is low, the interface is very prone to be debonded during stress and strain localization. Consequently, a narrow flaw between these inclusions can be enlarged and propagated during the tensile testing. As seen in Fig. 14 (Ti and O subfigures), it can be seen that the O element is accumulated in peripheral regions of the crack, while the Ti element keeps its form as an elongated phase at the centre of the crack. By considering the other elemental maps (like

Table 2
The average grain size for each variation of specimens.

Sample	LPBF-40A	LPBF-50A	LPBF-40B	LPBF-50B	LPBF-40C	LPBF-50C
Average Grain size (μm)	10.0	9.0	10.5	10.0	4.5	5.0

The associated error was measured to be ±0.5 μm.

Ni, Co, Fe), it can be concluded that the initial site for this debonding is the Al_2O_3/TiN interface; however, tensile strain leads to flaw expansion and propagation as a form of internal crack. Dislocations' pile up behind the crack and adjacent to its tip in the STEM-BF subfigure also confirms stress accumulation causing further propagation of this defect. In terms of cracking susceptibility, the grains with growth direction normal to the {100} plane are more vulnerable to crack nucleation and propagation, which is in agreement with the ODF maps in Fig. 8, [24] [35]. As a result, the TiN inclusions are nucleation sites of cracks, and subsequently, the fracture is accelerated [38].

Another feature depicted in Fig. 13 is the cellular structure. A trace of microsegregation in the Ti and Mo distribution maps is observable in a hexagonal shape. These elements, due to low distribution coefficient (k_0) and high diffusion coefficient (D_L) in liquid Fe, are more prone to be rejected to solid/liquid interface during solidification than those with high k_0 and low D_L, e.g. Ni and Mn [39] [40]. Despite Ti alloying element that tends to segregate into cell boundaries [14], Ni, Co, and Mo atoms are more prone to be interstitially trapped into the lattice, also known as solute trapping or banding effect [41]. Fast solid/liquid interface velocity and high cooling rate during the LPBF technique intensify the reluctance of solute segregation during solidification in which most of the solute atoms tend to be trapped into the matrix [42]. The Ni, Co, and Mo atoms can be thermodynamically solid solutionized into the matrix at low cooling rates. However, due to the fast solidification during the AM process, they will be dispersed over the entire microstructure showing trapping phenomenon. Furthermore, Ti shows intercellular segregation due to its low distribution coefficient and high diffusion coefficient [28].

Each alloying element has a different segregation rate depending on the concentration of the element in solid ($C_{s,i}$) and liquid ($C_{l,i}$) phases known as the distribution coefficient defined in Eq. (1). A solid/liquid interface velocity (R) is considered in the non-equilibrium case leading to Eq. (2). [28]

$$k_{0,i} = \frac{C_{S,i}}{C_{L,i}} \tag{1}$$

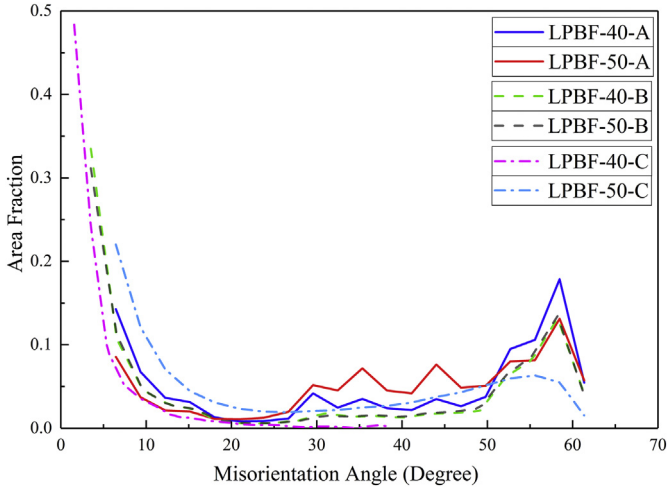

Fig. 12. Misorientation angle distribution in different zones of the LPBF-40 and LPBF-50 samples.

$$k_{R,i} = \frac{[k_{0,i} + (a_0 R/D_{L,i})]}{[1 + (a_0 R/D_{L,i})]} \tag{2}$$

where a_0 is the interatomic distance constant and $D_{L,i}$ is the diffusivity of element i in the interface. The distribution coefficients for Ni, Co, Mo and Ti are reported to be 0.81–0.95, 0.91–0.95, 0.57–0.61 and 0.30–0.32 respectively [43].

4. Discussion

4.1. Phase transformation

Martensitic transformation of the metastable γ phase needs a driving force to overcome the Gibbs energy barrier, also known as the saddle point in $\Delta G_{\gamma\rightarrow\acute{\alpha}}$ diagram. In 18Ni-300 maraging steel, except the ά phase formed via γ → ά athermal transformation, the rest of martensite is formed from the transformation of the metastable retained γ, where the driving force at room temperature is provided by strain induction [44] [45]. Since the X-ray has a high interaction volume in the XRD analysis, the phase fraction results present better statistics. As a result, the phase fraction studies are conducted using the XRD technique and results from Fig. 6 shows the elimination of the γ phase after uniaxial tensile deformation. As shown in Fig. 13, the cell boundaries are indicated as hexagonal cells in the Ti distribution map, where the corresponding zones in the STEM-BF contain a higher density of dislocations generated and piled due to the plastic deformation.

Retained austenite tends to remain along the cell boundaries due to the high concentration of austenite stabilizer alloying elements in these regions. Jagle et al. [46] and Liu et al. [47] showed that the ultra-low carbon steels show less hardenability in regions containing high contents of Ti, Mo, and Ni, which means that Ti in these steels can also act as γ stabilizer. A higher density of dislocations in the retained austenite can be due to the higher ability of strain hardening in γ rather than ά, which brings further nucleation of dislocations. A higher density of LAGBs in Fig. 9 (zone C) has resulted from the dislocation movements, also observed by Liu et al. [48]. Fig. 10 shows a higher mean value of KAM angles in the deformed samples, as another indication of the dislocations pile-up. In this case, increasing the dislocations density can occur in either the cell boundaries or during strain-induced martensitic transformation [49]. The graph of the misorientation angle in Fig. 12 shows peaks close to 60°. These peaks indicate twin misorientation in the γ phase [49], and the drop after deformation is attributed to phase transformation during plastic deformation. Since twinning occurs in the γ phase at the beginning of deformation, the possibility of mechanical twinning is reduced, as γ → ά further takes place [50].

4.2. Plastic deformation

The ά phase has higher flow stress than the γ phase. Under tensile loading, the γ ductile phase embedded into the martensitic matrix is the first one experiencing the plastic deformation [45]. Moreover, it is known that in the austenite phase, the dislocation density increases with strain [51]. In the BCC ά phase with high Peierls stress, the slip planes are less activated compared to the FCC phase containing lower Peierls stress. In maraging steels with intrinsically low stacking fault energy (SFE) due to the presence of various solute atoms of alloying elements within the lattice (Suzuki effect [52]), high Peierls stress of ά phase remarkably reduces the strain hardening rate of ά compared to the γ phase. During plastic deformation, the active slip systems of the FCC γ phase (⟨110⟩ {111}) and BCC ά phase (⟨111⟩ {110}{112}{123}) can be observed as shear deformation component in texture analyses. A weak γ-fibre as a shear deformation component in the FCC structure is observed in zones A and B (Figs. 5 and 7). In the severely deformed area in zone C, θ-fibre and γ-fibre components show higher intensities, which is showing the transformation of the austenite phase into martensite through the deformation.

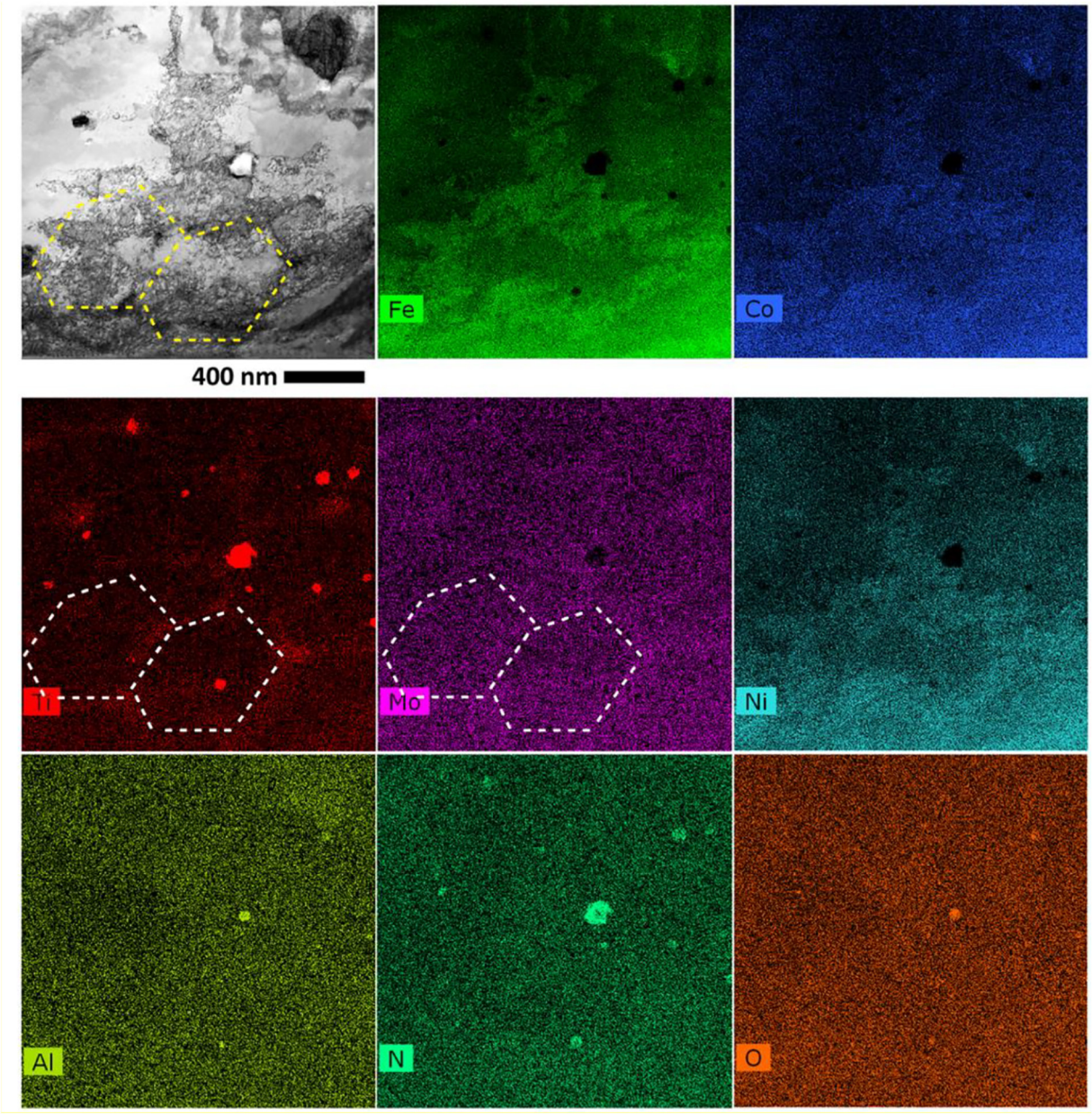

Fig. 13. STEM-BF image and corresponding elemental distribution maps in the LPBF-40-C sample.

In Fig. 10, higher KAM intensity in zone C represents higher localized strain, which occurs along the grain boundaries. The γ → ά transformation and the grain refining happen concurrently in zone C, which is confirmed in Fig. 11. Zone B, on the other hand, shows no significant change in the grain size compared to initial grains in the as-built structure (zone A). It is concluded that zone B is not subjected to large deformation, and consequently, the strain-induced phase transformation. It is noteworthy that the deformation occurs under the quasi-static state with no external heat source. As a result, the martensitic transformation is not followed by an irreversible ά → $\gamma_{Reverted}$ transformation. Therefore, the XRD pattern of the severely deformed sample does not show any γ phase.

The LAGBs distribution and misorientation correlation through plastic deformation are observed in Figs. 9 and 12 [53]. The misorientation angle shows multiple peaks that start from 30° and reach a maximum value close to 60°. During the deformation, the graphs become gentler, but the gradual increase within 30°-60° is still apparent. These graphs show the softening trend similar to rolled steels [48].

4.3. Strain hardening

Fig. 3 shows two stages of strain hardening through the total deformation. In stage I, between the yield strength (YS) and UTS, where the samples are exposed to homogeneous plastic deformation, the strain hardening values are positive; however, the trend of $d\sigma/d\varepsilon$ vs. ε is descending. The positive values are resulted from an increase in the number of dislocations, the more resistance against the dislocations mobility and further deformation, while the descending behaviour can be attributed to progress in strain-induced martensitic transformation [54]. The austenite phase in stage I is a source of mechanical twin generation [55]. Twins act as obstacles against dislocations movement on the slip planes. As a result, the structure still keeps strain hardening. On the other side, since the ά phase contains a considerable number of dislocations, its under-load lattice is saturated by stored energy. An increase in the density of dislocations lowers the rate of strain hardening. Therefore, progress in γ → ά transformation brings less strain hardening due to an increase in ά volume fraction. Shear bands result in the generation of

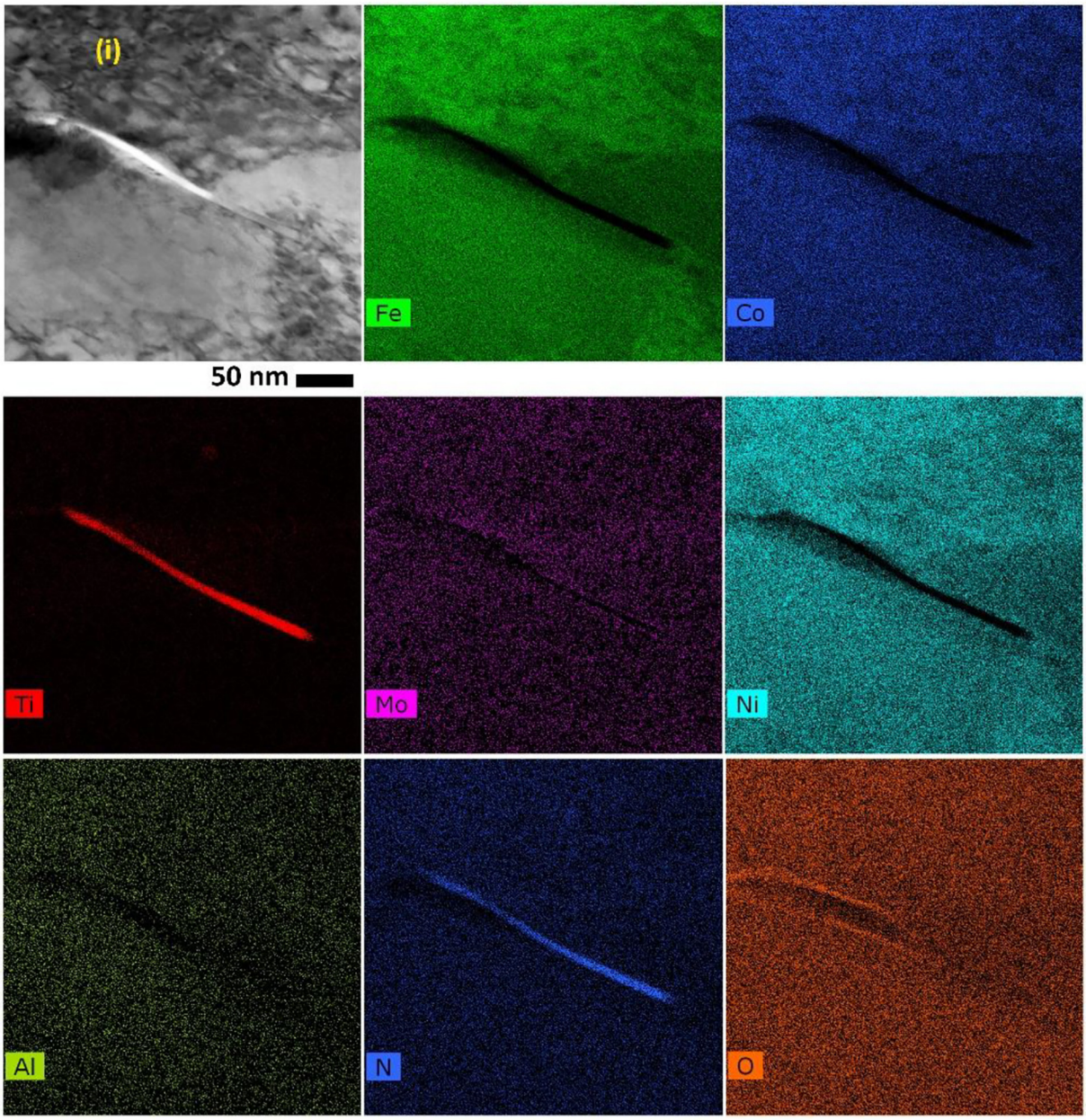

Fig. 14. STEM-BF image and corresponding elemental distribution maps in the LPBF-50-C sample (i: dislocations).

mechanical twins and stacking faults in the $\gamma_{\{111\}}$ planes, which are followed by the $\acute{\alpha}$ phase nucleation [56] [57]. After the peak stress in which $d\sigma/d\varepsilon = 0$, the fully martensitic structure is subjected to geometric softening caused by the necking effect. Hence, strain softening will be dominant and leads $d\sigma/d\varepsilon$ becoming negative.

In Fig. 10, the high-intensity KAM distribution in zone C shows that high dislocation density spreads along with the material. Besides, the austenite is first to deform, and the dislocations are formed and piled-up at the austenite phase along the cell boundaries. Since the austenite is distributed evenly all over the microstructure, local dislocation movements lead to localized strain rate increase followed by localized temperature increase [58] [59]. This process is followed by void formation and coalescence of microcracks and a reduction in the active cross-section, the so-called necking effect. It is noteworthy that the deformation occurs in a quasi-static state without an external heat source involved in the current study. Nevertheless, the dislocation motion provides the energy source to local heating, resulting in adiabatic shear band failure. The strain hardening is observed at a negative rate in this stage in Fig. 3.

5. Conclusions

A comprehensive study on deformation, strain hardening mechanisms, and strain-induced phase transformation of the AM 18Ni-300 maraging steel are conducted. The most important findings of this study can be mentioned as

- After the athermal $\gamma \rightarrow \acute{\alpha}$ transformation during the LPBF process, the retained γ mostly remains along the cell boundaries, the areas enriched by the solute atoms rejected during melting/solidifying repetitive cycles. In terms of segregated atoms, Ti and Mo atoms reveal a higher tendency of rejection during solidification and accumulation in cell boundaries. It is related to the low distribution coefficient and high diffusion rate of these atoms into the liquid Fe.

- Strain-induced γ → ά transformation is responsible for the variation of strain hardening rate under uniaxial tensile testing, where more strain hardening tendency of the retained γ compared to ά brings positive values of $d\sigma/d\varepsilon$ over stage I; however, progress in the martensitic transformation lowers the values down to zero at peak stress. After this point, in stage II, negative values of $d\sigma/d\varepsilon$ are assigned to geometric softening effect.
- The material adjacent to the fracture area (zone C) shows a fully martensitic structure, fine grains, a high fraction of LAGBs, a severe intensity of KAM angles, and a high density of dislocations at the vicinity of cell boundaries. In this regard, the AM sample manufactured by deposition of 40 μm-thick powder layers shows a lower fraction of LAGBs, and consequently, higher resistance against the dislocations slip during plastic deformation. Higher strain hardenability and UTS value in the LPBF-40 sample are due to this difference.

Data availability

The raw data required to reproduce the findings of this work cannot be shared at this time as the data also forms part of an ongoing study.

Declaration of Competing Interest

The authors declare that they have no known competing financial interests or personal relationships that could have appeared to influence the work reported in this paper.

Acknowledgement

The authors thank the following institutions for the provided funding for this work; Natural Sciences and Engineering Research Council of Canada (NSERC) grant number RGPIN-2016-04221, New Brunswick Innovation Foundation (NBIF) grant number RIF2017-071, Atlantic Canada Opportunities Agency (ACOA)- Atlantic Innovation Fund (AIF) project number 210414, Mitacs Accelerate Program grant number IT10669. The authors would also thank Victoria Jarvis and Dr. Jim Britton from McMaster Analytical X-Ray Diffraction Facility (MAX). The authors thank David Slimowitz from Additive Metal Manufacturing (AMM) in Concord, Ontario, for manufacturing the samples.

References

[1] W. Sha, Z. Guo, Maraging Steels, Modeling of Microstructure, Properties and Applications, Woodhead Publishing, 2009.
[2] V. Rajkumar, N. Arivazhagan, Role of pulsed current on metallurgical and mechanical properties of dissimilar metal gas tungsten arc welding of maraging steel to low alloy steel, Mater. Des. 63 (2014) 69–82.
[3] N. Shamsaei, A. Yadollahi, L. Bian, S.M. Thompson, An overview of direct laser deposition for additive manufacturing; part II: mechanical behavior, process parameter optimization and control, Addit Manufact. 8 (2015) 12–35.
[4] M. Mohammadi, H. Asgari, Achieving low surface roughness AlSi10Mg_200C parts using direct metal laser sintering, Addit Manufact. 20 (2018) 23–32.
[5] C. Tan, K. Zhou, W. Ma, P. Zhang, M. Liu, T. Kuang, Microstructural evolution, nanoprecipitation behavior and mechanical properties of selective laser melted high-performance grade 300 maraging steel, Mater. Des. 134 (2017) 23–34.
[6] J. Suryawanshi, K.G. Prashanth, U. Ramamurty, Tensile, fracture, and fatigue crack growth properties of a 3D printed maraging steel through selective laser melting, J. Alloys Compd. 725 (2017) 355–364.
[7] E. Cyr, H. Asgari, S. Shamsdini, M. Purdy, K. Hosseinkhani, M. Mohammadi, Fracture behaviour of additively manufactured MS1-H13 hybrid hard steels, Mater. Lett. 212 (2018) 174–177.
[8] X. Xu, S. Ganguly, J. Ding, S. Guo, S. Williams, F. Martina, Microstructural evolution and mechanical properties of maraging steel produced by wire+ arc additive manufacture process, Mater. Charact. 143 (2018) 152–162.
[9] A.G. Dos Reis, D.A.P. Reis, A.J. Abdalla, J. Otubo, High-temperature creep resistance and effects on the austenite reversion and precipitation of 18 Ni (300) maraging steel, Mater. Charact. 107 (2015) 350–357.
[10] ASM International Handbook Committee, Properties and Selection: Irons Steels and High Performance Alloys, ASM Handbook, Materials Information Company, America, 1991.
[11] E.A. Jägle, P.P. Choi, J. Van Humbeeck, D. Raabe, Precipitation and austenite reversion behavior of a maraging steel produced by selective laser melting, J. Mater. Res. 29 (17) (2014) 2072.
[12] L. Yuan, D. Ponge, J. Wittig, P. Choi, J.A. Jiménez, D. Raabe, Nanoscale austenite reversion through partitioning, segregation and kinetic freezing: example of a ductile 2 GPa Fe–Cr–C steel, Acta Mater. 60 (6–7) (2012) 2790–2804.
[13] M.M. Wang, C.C. Tasan, D. Ponge, A. Kostka, D. Raabe, Smaller is less stable: size effects on twinning vs. transformation of reverted austenite in TRIP-maraging steels, Acta Mater. 79 (2014) 268–281.
[14] S. Shamsdini, S. Shakerin, A. Hadadzadeh, B.S. Amirkhiz, M. Mohammadi, A trade-off between powder layer thickness and mechanical properties in additively manufactured maraging steels, Mater. Sci. Eng. A 776 (2020) 139041.
[15] S. Martin, S. Wolf, U. Martin, L. Krüger, D. Rafaja, Deformation mechanisms in austenitic TRIP/TWIP steel as a function of temperature, Metall. Mater. Trans. A 47 (1) (2016) 49–58.
[16] E. Emadoddin, A. Akbarzadeh, R. Petrov, L. Kestens, H. Pirgazi, Influence of cold-rolling reduction on retained austenite texture in cold-rolled and intercritically annealed TRIP-assisted steel, J. Appl. Crystallogr. 44 (6) (2011) 1190–1197.
[17] E.I. Galindo-Nava, P.E.J. Rivera-Díaz-del-Castillo, A model for the microstructure behaviour and strength evolution in lath martensite, Acta Mater. 98 (2015) 81–93.
[18] L. Morsdorf, C.C. Tasan, D. Ponge, D. Raabe, 3D structural and atomic-scale analysis of lath martensite: effect of the transformation sequence, Acta Mater. 95 (2015) 366–377.
[19] S. Shakerin, A. Hadadzadeh, B.S. Amirkhiz, S. Shamsdini, J. Li, M. Mohammadi, Additive manufacturing of maraging steel-H13 bimetals using laser powder bed fusion technique, Addit Manufact. 100797 (2019).
[20] H. Asgari, C. Baxter, K. Hosseinkhani, M. Mohammadi, On microstructure and mechanical properties of additively manufactured AlSi10Mg_200C using recycled powder, Mater. Sci. Eng. A 707 (2017) 148–158.
[21] A. Hadadzadeh, C. Baxter, B.S. Amirkhiz, M. Mohammadi, Strengthening mechanisms in direct metal laser sintered AlSi10Mg: comparison between virgin and recycled powders, Addit Manufact. 23 (2018) 108–120.
[22] M. Ahmed, A. Ali, S.K. Hasnain, F.H. Hashmi, A.Q. Khan, Magnetic properties of maraging steel in relation to deformation and structural phase transformations, Acta Metall. Mater. 42 (3) (1994) 631–638.
[23] M. Béreš, L. Wu, L.P.M. Santos, M. Masoumi, F.A.M. da Rocha Filho, C.C. Da Silva, H.F.G. de Abreu, M.G. Da Silva, Role of lattice strain and texture in hydrogen embrittlement of 18Ni (300) maraging steel, Int. J. Hydrog. Energy 42 (21) (2017) 14786–14793.
[24] N.C. Figueiredo, C.A.S. de Oliveira, M. Masoumi, H.F.G. de Abreu, Microstructural variations at different distance from the surface in forged 18 Ni C300 maraging steel, J. Mater. Res. Technol. 8 (1) (2019) 284–291.
[25] EOS Maraging Steel MS1,Material data sheet. , EOS GmbH, Munchen, 2017.
[26] Standard Test Methods for Tension Testing of Metallic Materials, Designation: E8/E8M-15a. , ASTM Standards, 2015.
[27] A. Rusinek, J.A. Rodríguez-Martínez, Thermo-viscoplastic constitutive relation for aluminium alloys, modeling of negative strain rate sensitivity and viscous drag effects, Mater. Des. 30 (10) (2009) 4377–4390.
[28] S. Dehgahi, M.H. Ghoncheh, A. Hadadzadeh, M. Sanjari, B.S. Amirkhiz, M. Mohammadi, The role of titanium on the microstructure and mechanical properties of additively manufactured C300 maraging steels, Mater. Des. 194 (2020) 108965.
[29] L.Z.I. Kučerová, A. Jandová, M. Bystrianský, Microstructural characterisation and in-situ straining of additive-manufactured X3NiCoMoTi 18-9-5 maraging steel, Mater. Sci. Eng. A 750 (2019) 70–80.
[30] T. Bhardwaj, M. Shukla, Effect of laser scanning strategies on texture, physical and mechanical properties of laser sintered maraging steel, Mater. Sci. Eng. A 734 (2018) 102–109.
[31] M. Sanjari, Y. He, E.J. Hilinski, S. Yue, L.A. Kestens, Texture evolution during skew cold rolling and annealing of a non-oriented electrical steel containing 0.9 wt% silicon, J. Mater. Sci. 52 (6) (2017) 3281–3300.
[32] F.D. Fischer, G. Reisner, E. Werner, K. Tanaka, G. Cailletaud, T. Antretter, A new view on transformation induced plasticity (TRIP), Int. J. Plast. 16 (7–8) (2000) 723–748.
[33] A. Pineau, A.A. Benzerga, T. Pardoen, Failure of metals I: brittle and ductile fracture, Acta Mater. 107 (2016) 424–483.
[34] M.D. Sangid, T. Ezaz, H. Sehitoglu, I.M. Robertson, Energy of slip transmission and nucleation at grain boundaries, Acta Mater. 59 (1) (2011) 283–296.
[35] M. Masoumi, H.F. Abreu, L.F. Herculano, J.M. Pardal, S.S. Tavares, M.J. Silva, EBSD study of early fractured phenomena in a 350 grade Maraging steel elbows exposed to hydrofluoric acid, Eng. Fail. Anal. 104 (2019) 379–387.
[36] L. Saraf, Kernel average misorientation confidence index correlation from FIB sliced Ni-Fe-Cr alloy surface, Microsc. Microanal. 17 (S2) (2011) 424–425.
[37] A.J. Schwartz, M. Kumar, B.L. Adams, D.P. Field, Electron Backscatter Diffraction in Materials Science, Springer, New York, 2009.
[38] U.K. Viswanathan, G.K. Dey, V. Sethumadhavan, Effects of austenite reversion during overageing on the mechanical properties of 18 Ni (350) maraging steel, Mater. Sci. Eng. A 398 (1–2) (2005) 367–372.
[39] R. Zhang, T. Jing, W. Jie, B. Liu, Phase-field simulation of solidification in multicomponent alloys coupled with thermodynamic and diffusion mobility databases, Acta Mater. 54 (8) (2006) 2235–2239.
[40] O. Hunziker, Theory of plane front and dendritic growth in multicomponent alloys, Acta Mater. 49 (20) (2001) 4191–4203.
[41] O. Dmitrieva, D. Ponge, G. Inden, J. Millán, P. Choi, J. Sietsma, D. Raabe, Chemical gradients across phase boundaries between martensite and austenite in steel studied by atom probe tomography and simulation, Acta Mater. 59 (1) (2011) 364–374.
[42] M.H. Ghoncheh, M. Sanjari, E. Cyr, J. Kelly, H. Pirgazi, S. Shakerin, A. Hadadzadeh, B. Shalchi Amirkhiz, L. Kentens, M. Mohammadi, On the solidification characteristics,

deformation, and functionally graded interfaces in additively manufactured hybrid aluminum alloys, Int. J. Plast. 133 (2020) 102840.
[43] Z.I. MORITA, T. TANAKA, Thermodynamics on the equilibrium distribution coefficients of solute elements between solid and liquid phases in iron alloys, Tetsu-to-Hagane 74 (7) (1988) 1210–1218.
[44] K. Tomimura, S. Takaki, Y. Tokunaga, Reversion mechanism from deformation induced martensite to austenite in metastable austenitic stainless steels, ISIJ Int. 31 (12) (1991) 1431–1437.
[45] K. Spencer, J.D. Embury, K.T. Conlon, M. Véron, Y. Bréchet, Strengthening via the formation of strain-induced martensite in stainless steels, Mater. Sci. Eng. A 387 (2004) 873–881.
[46] E.A. Jägle, Z. Sheng, P. Kürnsteiner, S. Ocylok, A. Weisheit, D. Raabe, Comparison of maraging steel micro-and nanostructure produced conventionally and by laser additive manufacturing, Materials 10 (1) (2017) 8.
[47] C. Liu, Z. Zhao, D.O. Northwood, Y. Liu, A new empirical formula for the calculation of MS temperatures in pure iron and super-low carbon alloy steels, J. Mater. Process. Technol. 113 (1–3) (2001) 556–562.
[48] Z. Liu, Q. Gao, H. Zhang, S. Luo, X. Zhang, W. Li, J. Y, H. Li, EBSD analysis and mechanical properties of alumina-forming austenitic steel during hot deformation and annealing, Mater. Sci. Eng. A 755 (2019) 106–115.
[49] M. Zhang, J. Wang, Y. Zhu, L. Zhang, P. Jin, Ex-situ EBSD analysis of hot deformation behavior and microstructural evolution of Mg–1Al–6Y alloy via uniaxial compression, Mater. Sci. Eng. A 775 (2020) 138978.
[50] S.H. Avner, Introduction to Physical Metallurgy, McGraw-hill, New York, 1974.
[51] A. Kundu, D.P. Field, P.C. Chakraborti, Effect of strain and strain rate on the development of deformation heterogeneity during tensile deformation of a solution annealed 304 LN austenitic stainless steel: An EBSD study, Mater. Sci. Eng. A 773 (2020) 138854.
[52] H. Suzuki, Segregation of solute atoms to stacking faults, J. Phys. Soc. Jpn. 17 (2) (1962) 322–325.
[53] S. Li, C. Guo, L. Hao, Y. Kang, Y. An, In-situ EBSD study of deformation behaviour of 600 MPa grade dual phase steel during uniaxial tensile tests, Mater. Sci. Eng. A 759 (2019) 624–632.
[54] Q. Zhu, C. Wang, H. Qin, G. Chen, P. Zhang, Effect of the grain size on the microtensile deformation and fracture behaviors of a nickel-based superalloy via EBSD and in-situ synchrotron radiation X-ray tomography, Mater. Charact. 156 (2019) 109875.
[55] P. Chowdhury, D. Canadinc, H. Sehitoglu, On deformation behavior of Fe-Mn based structural alloys, Mater. Sci. Eng. R. Rep. 122 (2017) 1–28.
[56] K.H. Lo, C.H. Shek, J.K.L. Lai, Recent developments in stainless steels, Mater. Sci. Eng. R. Rep. 65 (4–6) (2009) 39–104.
[57] A. Das, S. Sivaprasad, M. Ghosh, P.C. Chakraborti, S. Tarafder, Morphologies and characteristics of deformation induced martensite during tensile deformation of 304 LN stainless steel, Mater. Sci. Eng. A 486 (1–2) (2008) 283–286.
[58] S.D. Antolovich, R.W. Armstrong, Plastic strain localization in metals: origins and consequences, Prog. Mater. Sci. 59 (2014) 1–160.
[59] E. Nes, Modelling of work hardening and stress saturation in FCC metals, Prog. Mater. Sci. 41 (3) (1997) 129–193.